International Journal of Environmental Sciences
ISSN: 2229-7359
Vol. 11 No. 18s, 2025
https://theaspd.com/index.php

Synthesis, Characterization And Electrochemical Studies Of Zn Doped Mgfe$_2$o$_4$ Qds Via Co-Precipitation Technique

R.M.Regma Infant[1], **S.R. Gibin**[2,3], **Joselin Beaula T**[4,6], **J.Samuel**[5]
[1]Research Scholar, Department of Physics and Research Centre, Malankara Catholic College, Mariagiri, Kaliakkavilai-629153, Tamil Nadu, India.
[2]Formerly Assistant Professor, Department of Physics and Research Centre, Malankara Catholic College, Mariagiri – 629153, Tamil Nadu, India
[3]Associate Professor of Physics, Sree Sakthi Engineering College (Autonomous), Karamadai, Coimbatore-641104, Tamil Nadu, India
[4]Assistant Professor, Department of Physics and Research Centre, Malankara Catholic College, Mariagiri – 629153, Tamil Nadu, India
[5]Associate Professor of Physics, Cape Institute of Technology Levengipuram-627114, Tamil Nadu, India.
[6]Manonmaniam Sundaranar University, Abishekapatti-627012, Tirunelveli, Tamil Nadu, India.

Abstract

In this work, Zn-doped $MgFe_2O_4$ quantum dots (QDs) were synthesized using a cost-effective co-precipitation method. A thorough characterization was conducted utilizing XRD, FTIR, TEM, SEM, EDX, and XPS techniques. The analyses from XRD and FTIR confirmed the establishment of a well-defined spinel structure, while the XPS spectra validated the existence of Fe 2p, Mg 2p, O 1s, and Zn 2p elements. The TEM analysis demonstrated uniformly distributed quantum dots with an average particle size of 6.23 ± 0.18 nm. The electrochemical properties of the Zn-doped $MgFe_2O_4$ QDs were assessed through cyclic voltammetry (CV) and electrochemical impedance spectroscopy (EIS). The material displayed outstanding specific capacitance, favourable rate capability, and strong cycling stability. These results underscore the potential of Zn-doped $MgFe_2O_4$ QDs as promising electrode materials for high-performance supercapacitor applications.

Keywords: *Quantum dots, Co-precipitation technique, Spinel structure, Impedance, Supercapacitor.*

---

1. INTRODUCTION

In recent years, supercapacitors have accumulated significant interest from both researchers and industries Owing to their extensive range of applications, including hybrid electric vehicles, portable electronics, industrial backup systems, and military technologies. Their appeal lies in several key advantages, such as high-power density, extended cycle life, environmental compatibility, and enhanced safety [1]. As the global demand for energy continues to rise and concerns about fossil fuel depletion and eco-friendly materials for energy conversion and storage. Among the different energy storage technologies, supercapacitors (SCs) have surfaced as promising options due to their remarkable attributes, which include high power output, outstanding cycle stability, and improved safety. [4]. They possess a higher energy density compared to chemical power sources [4]. The efficiency of cost-effective and environmentally sustainable energy storage and conversion devices, such as batteries and electrochemical capacitors, is significantly affected by the physical and chemical properties of the electrode materials. As the world moves toward reducing dependence on fossil fuels, the development of advanced energy systems will play a vital role in meeting future energy demands [5, 6]. Nanoscale magnesium ferrite particles possess distinctive Characteristics that render them appropriate for a range of applications, including high-density data storage, high-frequency electronic components, and magnetic refrigeration systems [7]. The characteristics of electrode materials can be tailored by varying the precursor materials, synthesis techniques, and doping elements. Methods such as co-precipitation, combustion, spray pyrolysis, and other wet chemical approaches have been employed, each influencing the resulting morphology and, consequently, the electrochemical behaviour of the electrode material[8]. Among various synthesis methods, the non-aqueous co-precipitation approach is recognized for its simplicity and effectiveness. This technique significantly affects particle morphology, size, surface characteristics, and overall material properties. It also facilitates the formation of highly crystalline structures with uniform particle distribution. Quantum dots (QDs), in particular, they have become essential elements in both technological and electronic applications. In photoelectrochemical systems, QD-based photoanodes are capable of harvesting solar energy and converting it into electrical current, which can then be used to charge supercapacitor devices [9-13]. Quantum dots (QDs) with sizes typically near 10 nm have attracted significant interest due to their sharp and symmetric photoluminescence, adjustable emission wavelengths, intense brightness, and excellent photostability [9-11]. Quantum dots are engineered nanoscale structures that exhibit a high surface-to-volume ratio and distinct quantum confinement effects, along with several other remarkable features [14]. Their unique size-dependent properties have drawn considerable interest due to their outstanding optical, electronic, and structural behavior [15]. Due to the surface property of quantum dots the effectiveness of various applications, such as fuel cells, solar cells, photocatalysts, and antibacterial properties, can be enhanced [12-16]. Notably, nanoparticles with a spinel structure show considerable potential for energy storage solutions. When employed as electrode materials in lithium-ion batteries, metal ferrite nanoparticles can provide better electrical conductivity, a high specific capacity, improved electrochemical performance, and, crucially, economical energy generation [17]. Moreover, supercapacitors are gaining attention as a next-generation energy storage technology, delivering several benefits over traditional systems such as batteries and dielectric capacitors. Although element doping in magnesium ferrites has not been widely documented, existing studies indicate that nanoscale magnesium ferrites can be modified with various metal dopants to enhance their electrical, magnetic, optical, and electrochemical behavior. Among the transition metals, zinc (Zn) stands out due to its notable potential in electronic applications [18]. In this research, magnesium ferrite quantum dots doped with 0.01 M Zn were produced through an economical co-precipitation technique and then subjected to annealing at 700 °C.

To the best of our knowledge, this is the first report highlighting Zn-doped magnesium ferrite quantum dots treated at this specific temperature. This study aims to investigate the effects of incorporating Zn on the structural, morphological, electrochemical, surface area, and chemical characteristics of the synthesized quantum dots.

2.Experimental

2.1Synthesis of Zn doped $MgFe_2O_4$ QDs

Zn-doped $MgFe_2O_4$ quantum dots were produced through a modified co-precipitation technique, utilizing $MgFe_2O_4$ as the foundational material. All chemicals, sourced from Merck Chemicals, comprised $Mg(NO_3)_2{\cdot}4H_2O$, $Fe(NO_3)_3{\cdot}9H_2O$, and citric acid ($C_6H_8O_7$), each dissolved separately in 20 mL of deionized water. Sodium hydroxide (NaOH) was incrementally added to the mixed solution in a dropwise manner while continuously stirring at 80 °C for a duration of 30 minutes. Subsequently, 0.01 M zinc nitrate was incorporated, and the reaction mixture was stirred for an additional 3 hours at the same temperature. Citric acid functioned as a chelating agent, resulting in the formation of a brown precipitate. The obtained precipitate was extensively washed multiple times with deionized water and acetone to eliminate impurities. It was then dried at 80 °C, producing a dark brown powder. Ultimately, the dried sample underwent calcination at 700 °C for 3 hours in a muffle furnace to yield the final product.

2.2Characterization techniques

The X-ray diffraction (XRD) analysis was conducted to evaluate the crystalline phase of the Zn doped MgFe2O4 QDs using a BRUKER USA D8 Advance, Davinci instrument with CuKα radiation (λ = 1.54060 Å), operating at 40 kV and 30 mA. For characterization purposes, a scanning electron microscope (SEM) was employed, specifically the CAREL ZEISS EVO 18 model, after the sample was sputtered. The Transmission Electron Microscope (TEM) was utilized with the FEI – TECNAI G2 - 20 TWIN model (operating at 200 kV) to examine the morphology and ascertain the size. The Selected Area Electron Diffraction (SAED) pattern was acquired by placing the synthesized sample onto a carbon-coated copper grid. Elemental analysis was performed using Energy Dispersive X-ray Spectroscopy (EDX) with the Bruker EDX instrument featuring an LN2 free detector. X-ray photoelectron spectroscopy (XPS) measurements were executed using the ULVAC - PH1 INC model PH150000 version probe 111. The Brunauer Emmett Teller (BET) method was applied to assess the pore size and surface area using Quantachrome Instruments, Autosorb IQ series. Fourier transform infrared (FTIR) spectroscopy was conducted with the Purkin Elmer model Spectrum Two. To assess the electrochemical characteristics were examined through cyclic voltammetry (CV) utilizing a Versa STAT MC model.3. Results and discussion

3.1 XRD analysis

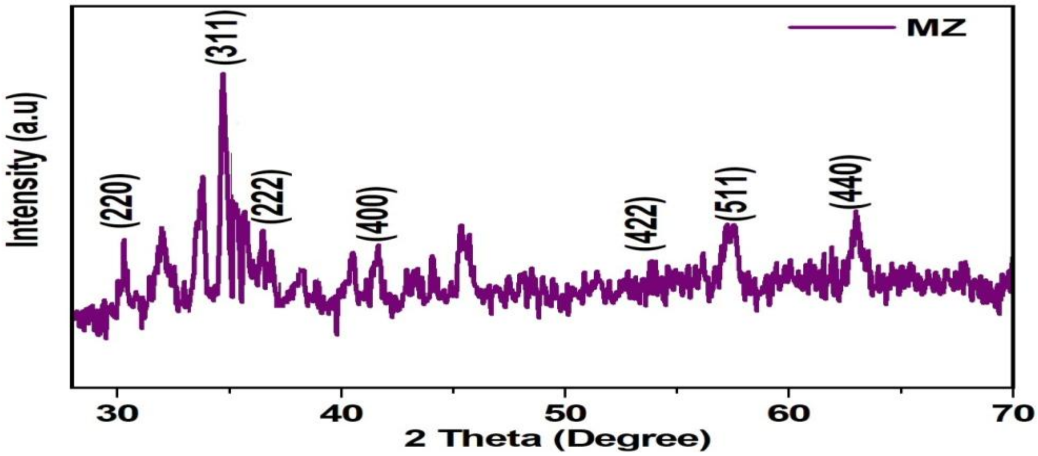

Fig. 1 X-ray diffraction patterns of Zn doped $MgFe_2O_4$ QDs

The crystalline characteristics of the samples prepared can be examined using X-ray diffraction (XRD). As illustrated in Fig. 1, the diffraction peaks for Zn-doped $MgFe_2O_4$ quantum dots (QDs) align well with the cubic spinel structure as per JCPDS card 01-1114 ($MgFe_2O_4$) [19]. The XRD patterns of the Zn-doped $MgFe_2O_4$ QDs synthesized via co-precipitation exhibit specific reflections at (220), (311), (222), (400), (422), (511), and (440), which are indicative of the Fd3m cubic spinel structure. The prominently intense peak observed for the (311) plane provides clear evidence of the cubic spinel ferrite structure in the produced sample. The average crystallite size of the Zn-doped $MgFe_2O_4$ QDs, corresponding to the diffraction peak (311), was calculated to be 9.27 nm using the Scherrer formula [20].

$$D = \frac{0.94\,\lambda}{\beta_D \cos\theta} \qquad \text{-----------}(1)$$

Where βD is the full width at half maximum (FWHM) of the diffracting peak, λ represents the wavelength of X-ray (0.1541 nm), and θ denotes the Bragg's diffraction angle.

3.2 TEM analysis

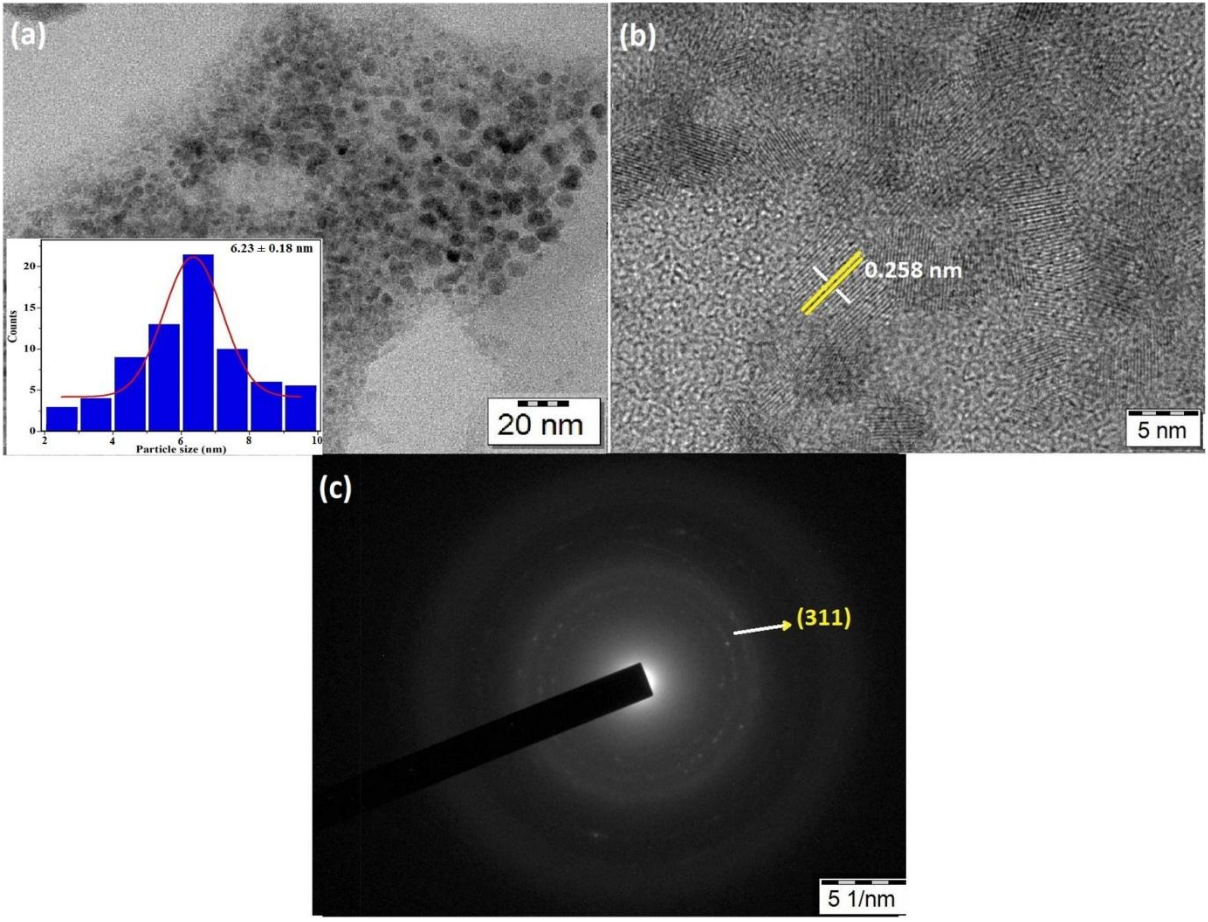

Fig. 2 (a) TEM micrographs (b) HRTEM image and (c) Selected area electron diffraction (SAED) pattern of Zn doped $MgFe_2O_4$ QDs

The morphology of the prepared sample was examined using transmission electron microscopy (TEM). The TEM image of the Zn-doped $MgFe_2O_4$ quantum dots (QDs) is presented in Fig. 2. Fig. 2 indicates that the Zn-doped $MgFe_2O_4$ consists of ultrafine spherical nanoparticles. The statistical particle size distribution diagram of the Zn-doped $MgFe_2O_4$ QDs, derived from the inset of Fig. 2(a), shows an average size of approximately 6.23 ± 0.18 nm. The lattice fringes of the crystalline Zn-doped $MgFe_2O_4$ QDs, as depicted in Figure 2(b), are illustrated in the high-resolution transmission electron microscopy (HRTEM) image. From the HRTEM image, the observable lattice fringe corresponding to the plane (311) measures about 0.258 nm, which is roughly comparable to the d311 value obtained from the X-ray diffraction (XRD) data. The diffraction rings observed in the selected area electron diffraction (SAED) pattern (Fig. 2(c)) align well with the standard data (JCPDS: 01-1114) for Zn-doped $MgFe_2O_4$ QDs [19]. The SAED pattern confirms the presence of circular rings indicative of the cubic spinel structure of Zn-doped $MgFe_2O_4$ QDs, with no additional rings detected.

3.3 SEM and EDX analyses

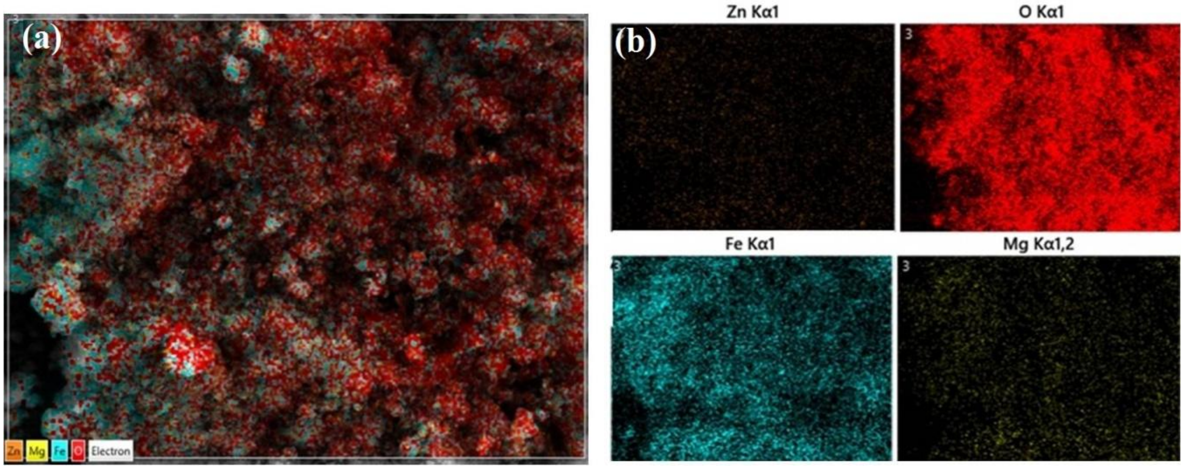

Fig. 3 (a) Scanning electron microscope (SEM) images and (b) Zn, Mg, Fe, and O in Zn doped $MgFe_2O_4$ QDs

Figure 3 illustrates the elemental mapping of the Zn-doped $MgFe_2O_4$ quantum dots (QDs). In the scanning electron microscopy (SEM) image (Figure 3 (a)), the particles are observed to be irregularly shaped and of varying sizes. Furthermore, the scanning transmission electron microscopy (STEM) image of the Zn-doped $MgFe_2O_4$ QDs (Figure 3 (b)) along with the corresponding elemental mapping indicates that the signals associated with Zn, Mg, Fe, and O exhibit a uniform spatial distribution. Figure 4 presents the results of the energy-dispersive X-ray (EDX) analysis performed on the Zn-doped $MgFe_2O_4$ QDs. From Figure 4, the atomic peaks of the elements zinc (Zn), iron (Fe), magnesium (Mg), and oxygen (O) are identified. The EDX results reveal the chemical composition (wt %) of Mg, Fe, O, and Zn to be 50.84 %, 32.28 %, 15.24 %, and 1.64 wt%, respectively. Additionally, the atomic percentages (%) are determined to be 41.52 %, 46.21 %, 11.12 %, and 1.15 % for Mg, Fe, O, and Zn, respectively. Minor peaks were also detected, which may be attributed to impurities from the sample holder of the instrument.

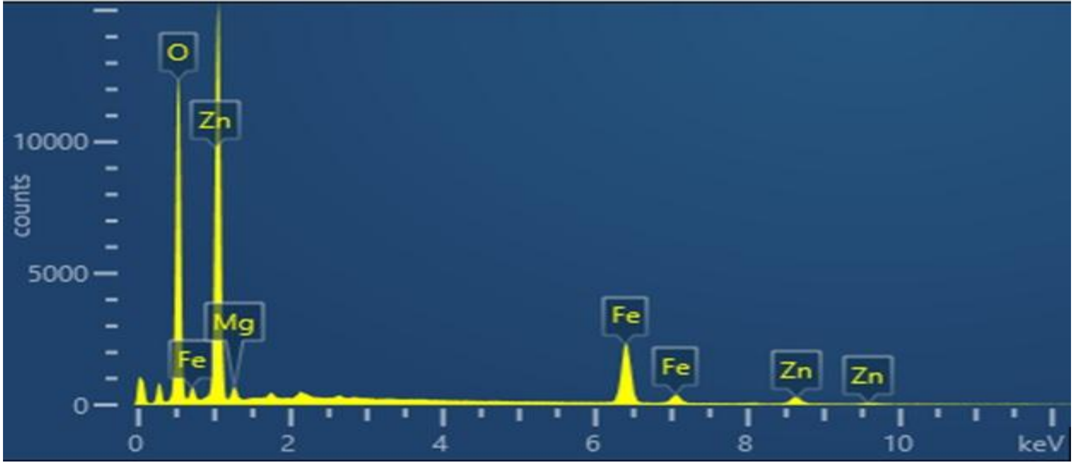

Fig.4 energy-dispersive x-ray spectrometer (EDX) elemental maps of the Zn doped $MgFe_2O_4$ QDs

3.4 XPS analysis

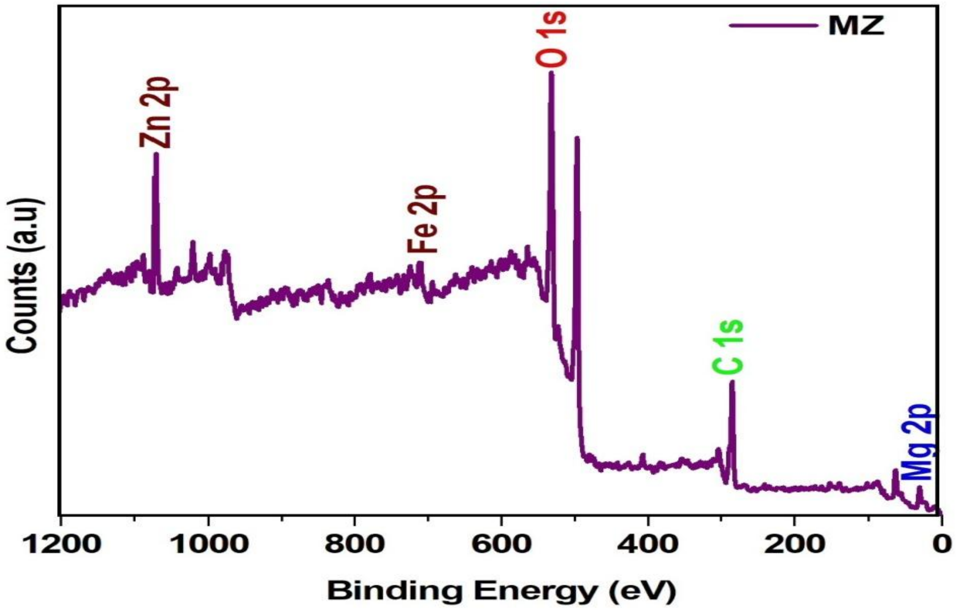

Fig. 5 X-ray photoemission survey spectrum of Zn doped $MgFe_2O_4$ QDs

X-ray photoelectron spectroscopy (XPS) was employed to gain a deeper insight into the surface compositions and chemical states of materials. Figure 5 illustrates the typical XPS survey spectra of the surface elements of Zn doped $MgFe_2O_4$ QDs, where the valence state and binding energy were ascertained from the XPS data. The XPS analysis revealed the complete spectrum of Zn doped $MgFe_2O_4$ nanoparticles, showcasing the presence of Zn, Fe, Mg, O, and carbon elements as depicted in Figure 5.

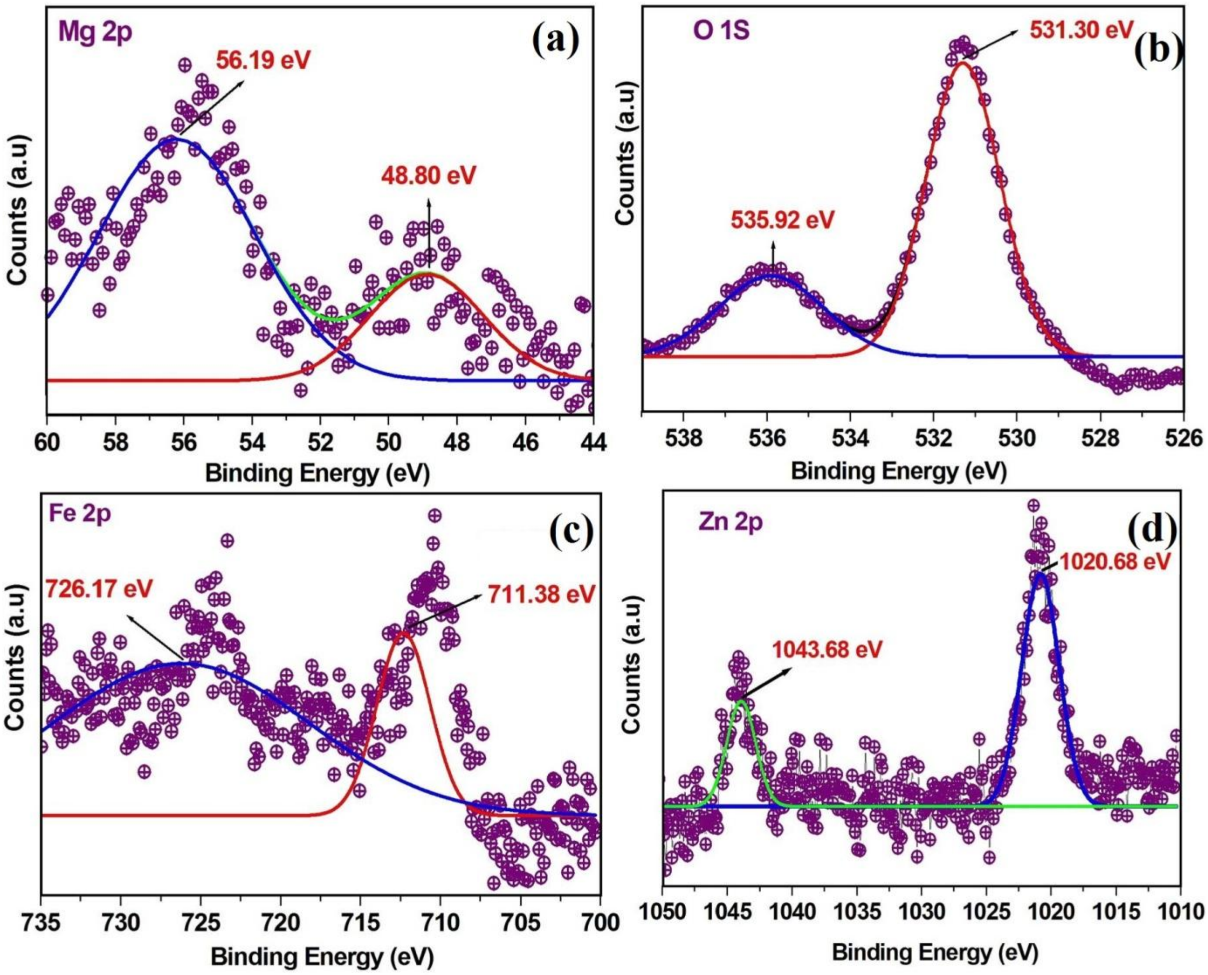

Fig. 6 XPS spectrum of (a) Mg 2p, (b) O 1s (c) Fe 2pand (d) Zn 2p

It has become a prevalent practice to utilize the C 1s signal identified at 284.26 eV from the adventitious carbon layer that is found on the majority of surfaces after exposure to air, serving as a binding energy reference [21]. Furthermore, the individual components of Zn doped $MgFe_2O_4$ quantum dots (QDs) were confirmed through specific X-ray photoelectron spectroscopy (XPS) spectra of Magnesium (Mg 2p3/2 and Mg 2p1/2), Oxygen (O 1s), Ferrous (Fe 2p1/2 and Fe 2p3/2), and Zinc (Zn 2p1/2 and Zn 2p3/2), as illustrated in Fig. 6 (a-d), respectively. The Mg 2p spectrum depicted in Fig. 6 (a) reveals the presence of Mg 2p3/2 and Mg 2p1/2 at 56.19 eV and 48.80 eV, respectively. The prominent peak at 56.19 eV corresponds to Mg within the $MgFe_2O_4$ lattice, indicating the complete oxidation of Mg in the sample [22]. The O 1s level is deconvoluted into two peaks as shown in Fig. 6 (d). The primary peak located at 535.92 eV is attributed to the O 1s level in the ZnO structure, while the peak at 531.30 eV is linked to the O 1s in the zinc hydroxide species [23]. For the Fe 2p (Fig. 5 (c)), core level peaks are observed at 711.38 eV (Fe 2p3/2) and 726.17 eV (Fe 2p1/2), respectively, indicating the presence of iron ions in the $MgFe_2O_4$ [24]. The Zn2p XPS spectrum of Zn doped $MgFe_2O_4$ QDs shows that the two peaks at binding energies of 1043.68 eV and 1020.68 eV correspond to Zn 2p1/2 and Zn 2p3/2, respectively, which signify the Zn2+ oxidation state in the Zn doped $MgFe_2O_4$ QDs phase [25]. The XPS results of the synthesized QDs indicate a spinal structure without the emergence of a secondary phase.

3.5 Brunauer - Emmett - Teller (BET)

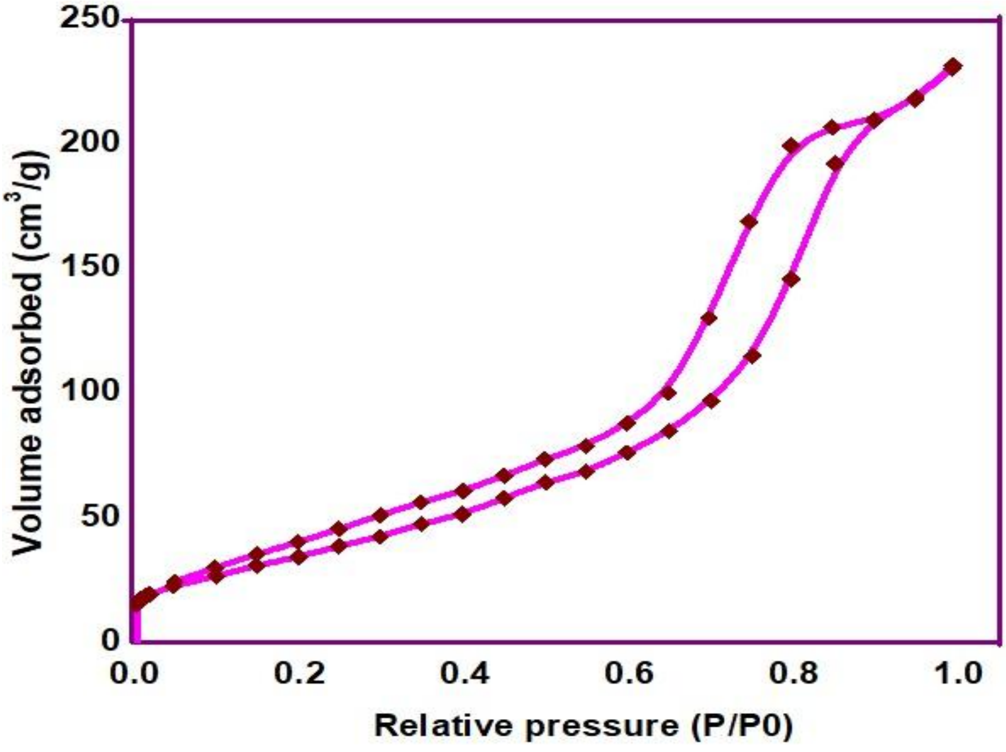

Fig. 7 N_2 adsorption-desorption isotherm of Zn doped $MgFe_2O_4$ QDs

N2 adsorption/desorption isotherms results of Zn doped $MgFe_2O_4$ QDs are shown in Fig. 7. The nitrogen adsorption isotherm demonstrates an IV-type with a H2 hysteresis loop according to the IUPAC classification based on the relative pressure (P/P0) [26, 27], the samples exhibit a bimodal pore distribution as determined by the Barrett-Joyner Halenda (BJH) method [28]. The analysis of the nitrogen adsorption isotherm indicates a notable BET surface area of 42.57 m2 g-1 for Zn doped $MgFe_2O_4$ QDs, which surpasses earlier findings regarding $MgFe_2O_4$ QDs [26]. The BJH pore-size distribution plots, illustrating adsorption dV(r) against pore radius, are presented in the inset of Fig. 8. These insets reveal that the predominant pore size within this system measures 2.213 nm, while the mesoporous range extends from 15 to 92 nm, suggesting a disorganized porosity structure. The BET results demonstrate that the synthesized Zn doped $MgFe_2O_4$ QDs serve as an effective nanomaterial, playing a crucial role in its super capacitive behavior.

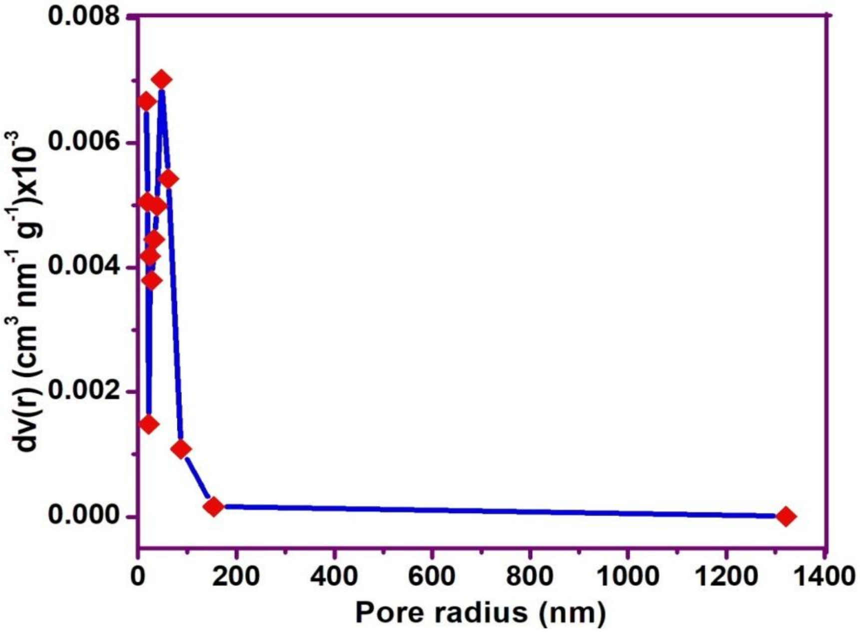

Fig. 8pore radius of Zn doped $MgFe_2O_4$ QDs

3.6. FTIR-spectra

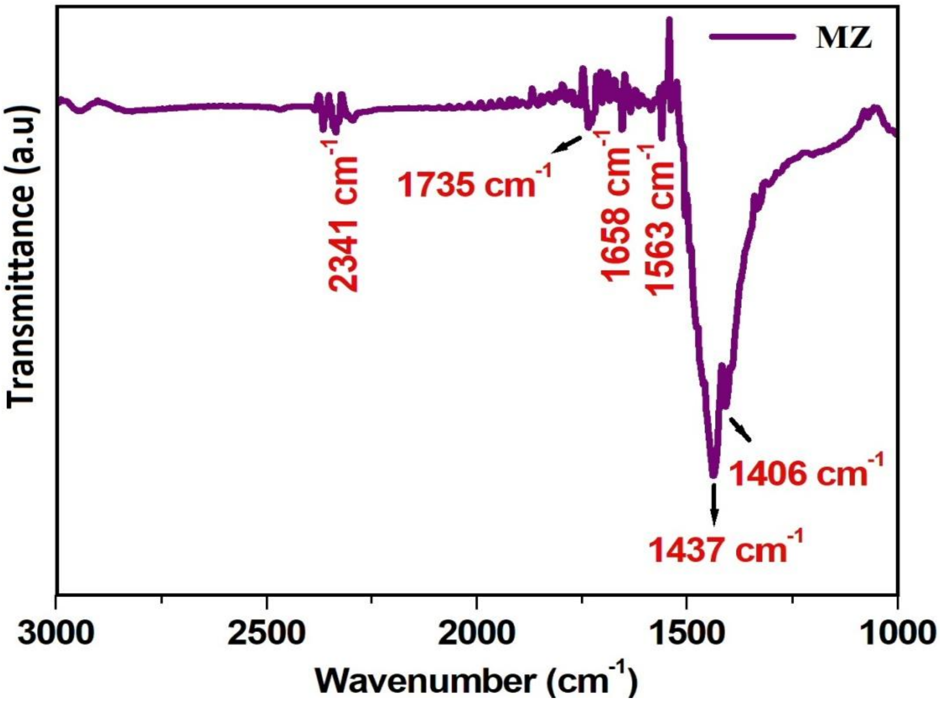

Fig. 9 FTIR spectrum of Zn doped $MgFe_2O_4$ QDs

The FT-IR transmittance spectrum of the synthesized sample, which was annealed at 700 °C for 3 hours, is illustrated in Fig. 9. The FTIR spectral analysis of the Zn-doped $MgFe_2O_4$ QDs confirms the formation of a spinel structure. The bands at 3000 cm^{-1} and 1000 cm^{-1} correspond to the stretching and bending vibrations of H–O–H, indicating the presence of free or absorbed water molecules in the samples. The peak at 2327 cm^{-1} signifies the O–H stretching vibration of the absorbed water molecule [29]. A high-frequency absorption peak was observed around 1737 cm^{-1}, confirming the presence of O–H groups in the prepared sample [30]. The peak at 1654 cm^{-1} is associated with the bending vibration of the H–O–H bond in water molecules [31]. The band at 1562 cm^{-1} relates to the C–H bending modes [32]. Furthermore, the band at 1434 cm^{-1} is attributed to the bending vibration associated with the CH2 groups [19].

3.7 Thermogravimetric and differential thermal analysis (TG/DTA)

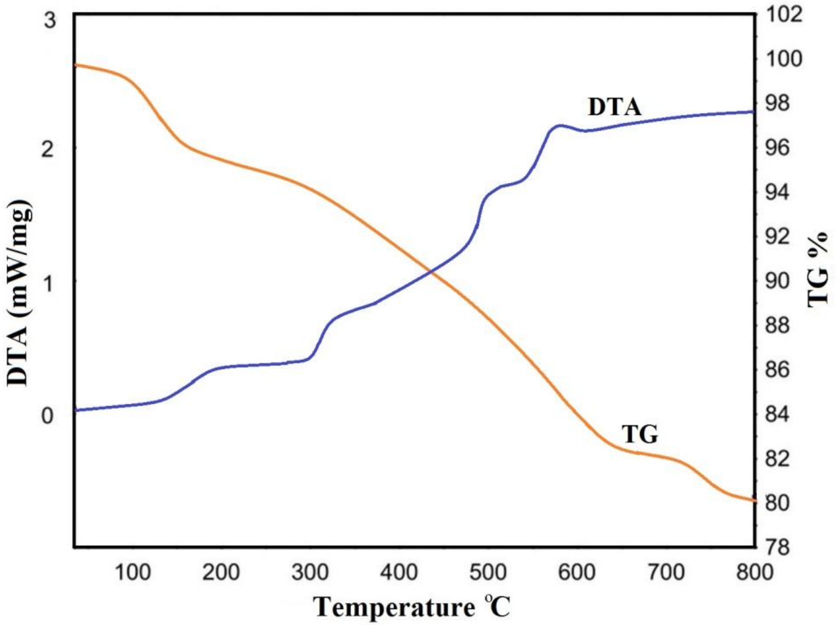

Fig. 10 TG/DT analysis curve of Zn doped $MgFe_2O_4$QDs.

The Zn doped $MgFe_2O_4$ QDs were subjected to simultaneous Thermogravimetric and differential thermal analysis (TG/DTA) in the temperature range between 35 ◦C and 850 ◦C. The Fig. 10 is illustrated the TG/DTA curve indicating the behaviour of the prepared sample. During the analysis, the first weight loss 3% was observed between 60 ◦C and 187 ◦C which is attributed to water dehydration due to the elimination of organic matter [33]. The 13 % weight loss was observed between 187 °C and 620 °C which is assigned to the decomposition of Mg- and Fe nitrates. Furthermore, the weight loss of around 3 % occurred at around 700 °C, which were related to the decay of organic templates present in the prepared sample [32]. The DTA curve shows endothermic peak around 92 °C, indicating the occurrence of dehydration. Additionally, exothermic peak at 320 °C was observed which suggests the decomposition of nitrates present in the sample [30].

3.8 Cyclic Voltammetry

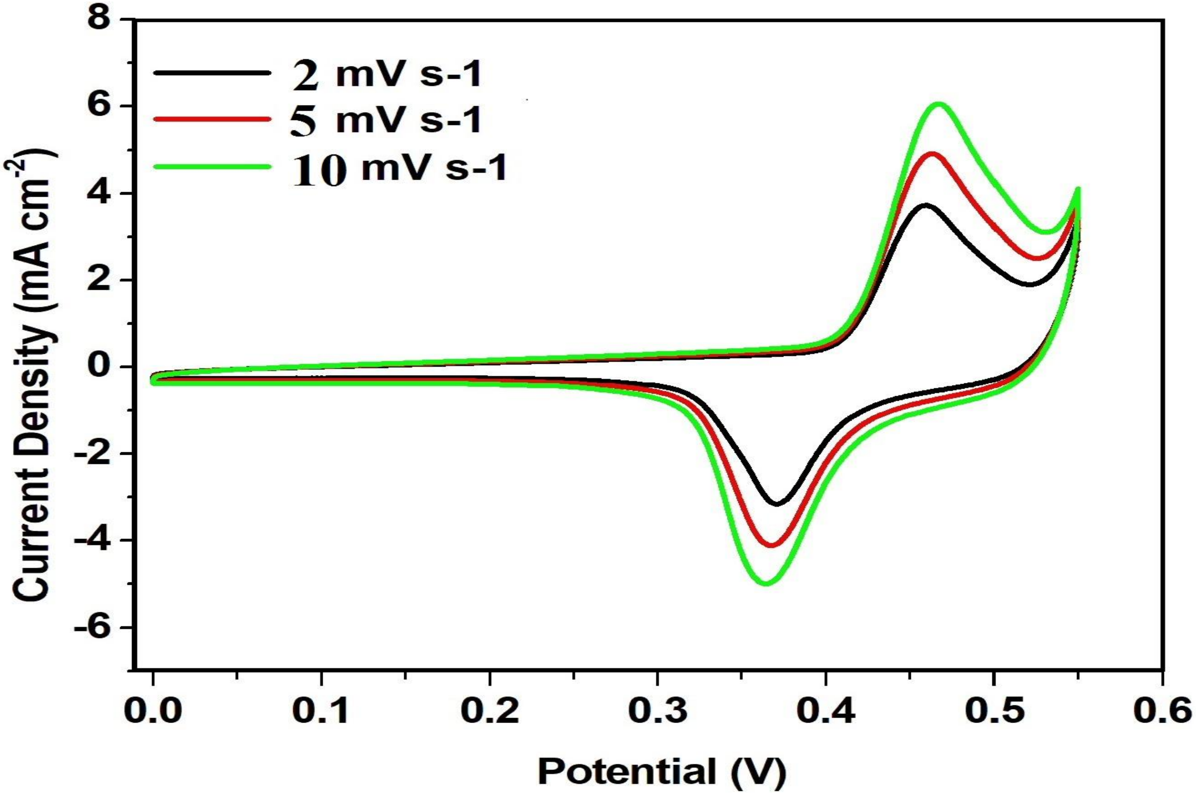

Fig. 12 CV pattern of Zn doped $MgFe_2O_4$ QDs

Electrochemical measurements were conducted by selecting a potential window that ranges from 0 to 0.6. Figure 12 illustrates the cyclic voltammetry (CV) curves at various scan rates of 2 mV/s, 5 mV/s, and 10 mV/s for Zn doped $MgFe_2O_4$ QDs. The CV patterns are plotted as current density against applied potential under visible light irradiation. Within the potential window of -0.0 to 0.6 V in 0.2 M tetra butyl ammonium perchlorate electrolyte solution, the Zn doped $MgFe_2O_4$ QDs electrode material demonstrated a series of pronounced faradaic redox peaks. At lower scan rates, the CV curves exhibit an almost rectangular shape, indicative of well-defined capacitive behaviour [17]. The CV patterns of the Zn doped $MgFe_2O_4$ QDs, which were calcined at 700 °C, reveal a pseudo-capacitive nature, as shown by the alterations in the CV curves with increasing scan rate [35]. As the scan rate increases, both the cathodic and anodic currents rise, confirming the reversible redox reaction of the electrode material [36]. The completion of the electrolytic process for an electrode material is determined by the applied potential [37]. This suggests the existence of pseudo-capacitive processes within the system, reflecting a dynamic capacitive response that is influenced by the scan rate. When the scan rate is increased, the cathodic and anodic current increased which ensured that the reversible redox reaction of the electrode material. The completion of electrolytic process of an electrode material is decided by the given potential [37]. This indicates the presence of pseudo-capacitive processes within the system, indicating a dynamic capacitive response influenced by the scan rate. The following equation is used to determine from the charge-discharge profile of the specific capacitances (Cs) value of the prepared Zn doped $MgFe_2O_4$ electrode [38]

$$Cs = Q/(\Delta v.m) \quad \text{-----------} \ (2)$$

Here, Q stands for the anodic and cathodic charges that are measured during each cyclic voltammetry (CV) scan, and C_s is the electrode material's specific capacitance. The constant scan rate (mVs^{-1}) used for the measurements is indicated by Δv, whereas the variable m represents the mass of the active electrode material (in milligrams). Every CV analysis was carried out within the 0.0–0.6 V range.

The Zn-doped $MgFeO_4$ CV profile's nearly perfect rectangular form indicates capacitive behavior and is linked to faradaic redox processes that take place at the active electrode's surface. Additional proof of the electrode material's pseudocapacitive properties is provided by the existence of two separate redox peaks [39]. The oxidation and reduction peak current densities rise in tandem with the scan rate as it increases from low to high values, as illustrated in Fig. 12. Peak positions also somewhat shift. Rapid and reversible redox reactions on the electrode surface because these shifts. Interestingly, the CV curves show good electrochemical reversibility, maintaining their shape without noticeable distortion, even at a relatively high scan rate of 10 mV s^{-1}.

One significant finding was that the specific capacitance was highest at the lowest scan rate. This suggests that electrolyte ions have enough time to penetrate the inner and outer surfaces of the porous electrode design at slower scan rates. Larger scan speeds, however, lead to less effective use of the electrode's active regions since ion transport is primarily restricted to the outer surface. Improved charge storage is made possible by the high mesoporous structure of $MgFe_2O_4$, which seems to increase the active surface area.

Therefore, electric double-layer capacitance and faradaic redox contributions are both involved in the charge storage process, with the latter being more important because of the pseudocapacitive nature. The electrode at 2 mV s^{-1} has the greatest capacitive double layer among the measured scan rates, suggesting efficient electron–hole separation and charge carrier transport at the electrode–electrolyte interface. For scan speeds of 2, 5, and 10 mV s^{-1}, the measured specific capacitance values are 284 Fg^{-1}, 191 Fg^{-1}, and 146 Fg^{-1}, respectively. For applications involving high-performance supercapacitors, this pattern shows that greater capacitance values can be obtained at lower scan rates, which is very beneficial.

3.9. Impedance analysis

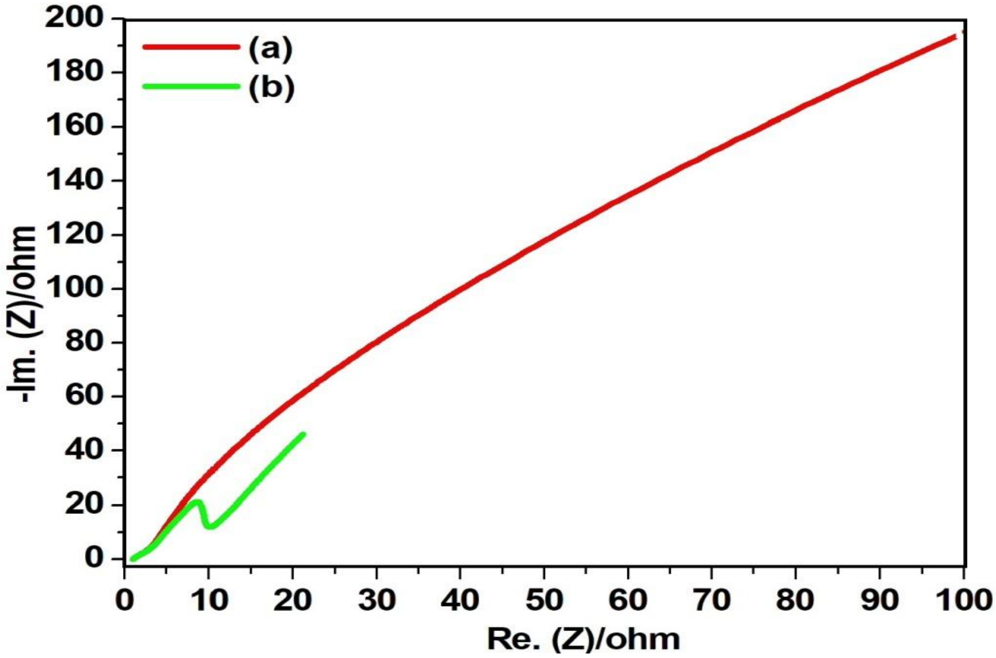

Fig. 11 Variation between Re. (Z) and –Im. (Z) of Zn doped $MgFe_2O_4$ QDs at different temperatures (a) 100 °C and (b) 150 °C

The electrochemical impedance spectroscopy (EIS) is a powerful technique for examining the electrical characteristics of Zn-doped $MgFe_2O_4$ electrode materials and their interfaces, including the electrode-electrolyte interface and temperature variations. EIS facilitates the differentiation of contributions from the material and interface, allowing for the investigation of ionic conductivity and dielectric relaxation processes within the electrolytes [40]. The Nyquist plots for Zn-doped $MgFe_2O_4$ electrodes are depicted in Fig. 11. This figure illustrates the correlation between the real and imaginary components of the complex impedance. Analysing both real and imaginary impedance provides insights into the existence of grains and grain boundaries. Consequently, conduction may occur over long or short distances, indicating either non-localized or localized charge transfer [41]. The Nyquist plots reveal that the system's impedance forms a semicircle, which is influenced by the applied potential. Additionally, it indicates that the intercept point on the real axis shifts with increasing temperature, implying a reduction in the material's resistive properties [42]. This analysis yields the bulk (Rb) and grain boundary (Rgb) resistances of the materials. This observation can be explained by the greater influence of grains compared to grain boundaries in zinc-doped magnesium ferrites [43]. The impedance results of Zn doped $MgFe_2O_4$ QDs provides the high conductivity and valuable insights into the selection of impedance devices and technologies.

4. CONCLUSION

In this research, Zn-doped $MgFe_2O_4$ quantum dots (QDs) were effectively synthesized using the co-precipitation method and extensively characterized through various analytical techniques. XRD analysis verified the creation of a single-phase cubic spinel structure with an average crystallite size of about 9.27 nm. TEM and HRTEM images demonstrated the existence of uniformly distributed, ultrafine spherical nanoparticles exhibiting well-defined lattice fringes. Elemental mapping and EDX analysis confirmed the uniform distribution of Zn, Mg, Fe, and O elements. XPS spectra further validated the oxidation states and chemical environments of the constituent, element supporting the formation of a pure spinel phase without secondary phases.

BET analysis revealed a notable surface area of 42.57 m^2/g along with a mesoporous structure, both of which are beneficial for electrochemical applications. FTIR and TG/DTA analyses confirmed the establishment of the spinel structure and assessed the thermal stability and compositional characteristics of the QDs. Electrochemical impedance spectroscopy illustrated a reduction in resistance at higher temperatures and emphasized the predominance of grain conductivity, which is essential for effective charge transport. Additionally, cyclic voltammetry demonstrated significant pseudocapacitive behaviour, achieving a maximum specific capacitance of 284 F/g at a scan rate of 2 mV/s, which signifies excellent electrochemical reversibility and substantial energy storage potential.

The findings collectively highlight the promise of Zn-doped $MgFe_2O_4$ quantum dots as effective electrode materials for high-performance supercapacitor applications, due to their advantageous structural, morphological, and electrochemical properties.

REFERENCE

1. N. Kitchamsetti, Y. R. Ma, P. M. Shirage and R. S. Devan, Mesoporous perovskite of interlocked nickel titanate nanoparticles for efficient electrochemical supercapacitor electrode, J. Alloys Compd., 833 (2020) 155134-155147.
2. G. Premanand, D.V. Sridevi, S. Perumal, T. Maiyalagan, J. D. Rodney and V. Ramesh, New hybrid semiconducting CdSe and Fe doped CdSe quantum dots based electrochemical capacitors, Mater. Sci. Eng. : B, 286 (2022) 116015-116027.
3. Z. H. Meng, W. Yan, M. Y. Zou, H. Miao, F. X. Ma, A. B. Patil, R. Yu, X. Y. Liu and N. B. Liu, Tailoring NiCoAl Layered Double Hydroxide Nanosheets for Assembly of High-performance Asymmetric Supercapacitors, Journal of Colloidal Interface Science, 583 (2021) 722–733.
4. Y. P. Gao and K. J. Huang, NiCo2S4 Materials for Supercapacitor Applications, Chemistry Asian Journal, 12 (2017) 1969–1984.
5. Y. Q. Du, P. Xiao, J. Yuan and J. W. Chen, Research Progress of Graphene-Based Materials on Flexible Supercapacitors, Coatings, 10 (2020) 892-901.
6. B. Chameh, M. Moradi, S. Hajati and F. A. Hessari, Design and Construction of ZIF (8 and 67) Supported Fe3O4 Composite as Advanced Materials of High Performance Supercapacitor, Physica E, 126 (2021) 114442-114449.
7. S. Thankachan, S. Xavier, B. Jacob, and E. M. Mohammed, , A comparative study of structural, electrical and magnetic properties of magnesium ferrite nanoparticles synthesised by sol-gel and co-precipitation techniques, J. Experimental Nanoscience, 8 (2013) 347–357.
8. M. Niederberger, Nonaqueous Sol-Gel Routes to Metal Oxide Nanoparticles, Acc. Chem. Res., 40 (2007) 793-800.
9. A. Tufani, A. Qureshi and J. H. Niazi, Iron oxide nanoparticles based magnetic luminescent quantum dots (MQDs) synthesis and biomedical/biological applications: A review, Mater. Sci. Eng. C, 118 (2021) 111545-111566.
10. K. B. Riad, S. V. Hoa and P. M. W. Adam, Metal Oxide Quantum Dots Embedded in Silica Matrices Made by Flame Spray Pyrolysis, ACS Omega, 6 (2021) 11411—11417.
11. A. Baldelli, H. Etayash, H. Oguzlu, R. Mandal, F. Jiang, R. E. W. Hancock and A. P. Singh, Antimicrobial properties of spray-dried cellulose nanocrystals and metal oxide-based nanoparticles-in-microspheres,Chem. Eng. J. Adv., 10 (2022) 100273-100287.
12. A. P. Litvin, I. V. Martynenko, F. P. Milton, A. V. Baranov, A. V. Fedorov and Y. K. Gunko, Colloidal quantum dots for optoelectronics, **J. Mater. Chem. A, 5** (2017) 13252-13275.
13. Y. L. Liu, Z. M. Liu, Y. Yang, H. F. Yang, G. L. Shen, and R. Q. Yu, Simple synthesis of MgFe2O4 nanoparticles as gas sensing materials, Sens. Actuators B, 107 (2005) 600–604.
14. R. Danish, F. Ahmed, B.H. Koo, Rapid synthesis of high surface area anatase titanium oxide quantum dots, Ceram. Int., 40 (2014) 12675–12680.
15. L. Zhu, W.J. An, J.W. Springer, L.B.M. Lopez, S. Gullapalli, D. Holten, M.S. Wong, P. Biswas, Linker-free quantum dot sensitized TiO2 photoelectrochemical cells, Int. J. Hydrogen Energy 37 (2012) 6422–6430.
16. L. Pan, J.J. Zou, S. Wang, Z.F. Huang, A. Yu, L. Wang, X. Zhang, Quantum dot self-decorated TiO2 nanosheets, Chem. Commun., 49 (2013) 6593–6595.
17. M. W. Mushtaq, M. Shahbaz, R. Naeem, S. Bashir, S. Sharif, K. Alia and N. A. Dogar, Synthesis of surfactant-assisted nickel ferrite nanoparticles (NFNPs@surfactant) to amplify their application as an advanced electrode material for high-performance supercapacitors, RSC Adv., 14 (2024) 20230-20240.
18. C. O. Ania, A. Gomis-Berenguer, J. Dentzer and C. Vix-Guterl, Nanoconfinement of glucose oxidase on mesoporous carbon electrodes with tunable pore sizes, J. Electroanal. Chem., 808 (2018) 372–379.
19. M. G. Naseri, M. H. M. Ara, E. B. Saion and A. H. Shaar, Super-paramagnetic magnesium ferrite nanoparticles fabricated by a simple, thermal-treatment method, J. Magnetism and Magnetic Mater., 350 (2014) 141–147.
20. J. Samuel, S. Suresh, S. Shabna, V. S. Vinita, N. J. Ananth, P.M.S. Shinu, A. Mariappan, T. simon, Y. Samson and C.S. Biju, Characterization and antibacterial activity of Ti doped ZnOnanorods prepared by hydrazine assisted wet chemical route, Physica E: Low Dimens. Syst. Nanostruct., 143 (2022) 115374-115385.
21. G. Greczynski and L. Hultman, C 1s peak of adventitious carbon aligns to the vacuum level: dire consequences for material's bonding assignment by photoelectron spectroscopy, Chem. Phys. Chem., 18 (2017)
22. O. P. Das and S. K. Pandey, Optical, Compositional and Electrical Properties of Transparent MgO Thin Film for ReRAM Devices, J. Phys., 2426 (2023) 012031-012038.
23. S. S. Guzman, B. R. Jayan, E. d. Rosa, A. T. Castro, V. G. Gonzalez and M. J. Yacaman, Synthesis of assembled ZnO structures by precipitation method in aqueous media, Mater.Chem. Phys., 115 (2009) 172-178.
24. M. Silva, V. Murzin, L. Zhang, J. Baltrus and J. Baltrusaitis, Transition Metal Doped MgO Nanoparticles for Nutrient Recycling: An Alternate Mg Source for Struvite Synthesis from Wastewater, Environmental Science: Nano, 7 (2020)3482–3496.
25. X. Ma, P. Zhang, Y. Zhao, Y. Liu, J. Li, J. Y. Zhou, X. Pan and E. Xie, Role of N doping on the electrochemical performances of $ZnCo_2O_4$ quantum dots/reduced graphene oxide composite nanosheets, Chem. Eng. J., 327 (2017) 1000–1010.
26. A. Monunith, A. Rajan and N. K. Sahu, Comparative study of enzymatic and non-enzymatic detection of glucose using manganese ferrite nanoparticles, Mater. Res. Express, 7 (2020) 1-9.
27. C. O. Ania, A. Gomis-Berenguer, J. Dentzer and C. Vix-Guterl, Nanoconfinement of glucose oxidase on mesoporous carbon electrodes with tunable pore sizes, J. Electroanal. Chem., 808 (2018) 372–379.
28. J. Samuel, J. E. shaji, S. S. J. Dhas, S. Suresh, V. S. Vinita and C.S.Biju, UV-blocking performance and antibacterial activity of Cd, Ba co-doped ZnOnanomaterials prepared by a facile wet chemical method, Surf. Interface Anal., 1 (2023) 1-14.

29. A. M. Jacintha, V. Umapathy, P. Neeraja and S. R. J. Rajkumar, Synthesis and comparative studies of $MnFe_2O_4$ nanoparticles with different natural polymers by sol–gel method: structural, morphological, optical, magnetic, catalytic and biological activities, J. Nanostruct. Chem., 7 (2017) 375–387.

30. M. M. N. Ansari, S. Khan and N. Ahmad, Effect of R^{3+} (R= Pr, Nd, Eu and Gd) substitution on the structural, electrical, magnetic and optical properties of Mn-ferrite nanoparticles, J. Magn. Magn Mater., 465 (2018) 81–87.

31. L. A. Kafshgari, M. Ghorbani and A. Azizi, Synthesis and characterization of manganese ferrite nanostructure by co-precipitation, sol-gel, and hydrothermal methods, Particulate Sci. Technol., 37 (2018) 904–910.

32. R. Sundari, T. I. Hua, M. Aziz and D. Nizar, The characterization study of ferrites (magnesium and manganese) using sol gel method, The Malaysian J. Analytical Sciences, 18 (2014) 485–490.

33. Z. Hammache, A. Soukeur, S. Omeiri, B. Bellal and M. Trari, Physical and photo-electrochemical properties of $MgFe_2O_4$ prepared by sol gel route: application to the photodegradation of methylene blue, J. Mater. Sci.: Mater. Electron., 30 (2019) 5375-5382.

34. L. Zhang, Y. Dai, C. Li, Y. Dang, R. Zheng, Z. Wang, Y. Wang, Y. Cui, H. Arandiyan, Z. Shao, H. Sun, Q. Zhuang and Y. Liu, Recent advances in electrochemical impedance spectroscopy for solid-state batteries, Energy Storage Mater., 69 (2024) 103378-103416.

35. K. Pradeeswari, A. Venkatesan, P. Pandi, K. Karthik, K.V. Hari Krishna and R. Mohan Kumar, Study on the electrochemical performance of ZnO nanoparticles synthesized via non-aqueous sol-gel route for supercapacitor applications, Mater. Res. Exp., 6 (2019) 105525-105532.

36. S. C. Pang, B. H. Wee and S. F. Chin, The capacitive behaviors of manganese dioxide thin-film electrochemical capacitor prototypes, Int. J. Electrochem., 2011 (2011).

37. D. Abisha, S. R. Gibin, V. K. PremKumar and A. Mariappan, Improved supercapacitor application of manganese ferrite nanoparticles via co-precipitation technique, Heliyon, 9 (2023) 21120-21131.

38. K. Sathishkumar, N. Shanmugam, N. Kannadasan, S. Cholan and G. Viruthagiri, Opto, magnetic and electrochemical characterization of $Ni_{1-x}Co_xO$ nanocrystals, J. Mater. Sci. Mater. Electron., 26 (2015) 1881–1889.

39. A. K. Behera, N. K. Mohanty, S. K. Satpathy, B. Behera and P. Nayak, Investigation of complex impedance and modulus properties of Nd doped $0{:}5BiFeO_3$–$0{:}5PbTiO_3$ multiferroic composites, Cent. Eur. J. Phys., 12 (2014) 851–861.

40. M. Kashif, M. E. Ali, S. M. U. Ali, U. Hashim and S. B. Abd Hamid, Impact of hydrogen concentrations on the impedance spectroscopic behavior of Pd-sensitized ZnO nanorods, Nanoscale Res. Lett., 8 (2013) 1–9.

41. S. K. Barik, R. N. P. Choudhary, P. K. Mahapatra, Impedance spectroscopy study of $Na_{1/2}Sm_{1/2}TiO_3$ ceramic, Appl. Phys. Mater. Sci. Process, 88 (2007) 217–222,

42. S. R. Gibin, P. Sivagurunathan, Synthesis and characterization of nickel cobalt ferrite ($Ni_{1-x}Co_x Fe_2O_4$) nano particles by co-precipitation method with citrate as chelating agent, J. Mater. Sci. Mater. Electron., 28 (2017) 1985–1996.

43.Ahmad Umar, Faheem Ahmed, Nabi Ullah, Sajid Ali Ansari, Shahid Hussain, Ahmed A. Ibrahim, Hussam Qasem, Sundararajan Ashok Kumar, Mohsen A. Alhamami, Noura Almehbad, Hassan Algadi, Tubia Almas, Amal F. Selim and Sotirios Baskoutas, Exploring the potential of reduced graphene oxide/polyaniline (rGO@PANI) nanocomposites for high-performance supercapacitor application, Electrochim. Acta, 479 (2024) 143743.